Projection deconvolution for proton CT using the spatially variant path uncertainty

Feriel Khellaf, Nils Krah, Jean Michel Létang, Simon Rit

Projection deconvolution for proton CT using the spatially variant path uncertainty

Feriel Khellaf, Nils Krah, Jean Michel Létang and Simon Rit

***Abstract*—Proton computed tomography (pCT) suffers from a lower spatial resolution compared to X-ray CT due to the stochastic non-linear proton paths. The most likely path (MLP) formalism provides an estimate for the proton path as well as the uncertainty around this estimate. Using the MLP estimate for the image reconstruction instead of straight integration lines has been shown to improve the spatial resolution of pCT images. In this work, the aim is to further increase the spatial resolution by also including the path uncertainty in the reconstruction algorithm. We proposed a projection-based deconvolution method, applied within the framework of a direct reconstruction algorithm based on distance-driven binning. We used an MLP formalism accounting for tracker resolution in addition to multiple Coulomb scattering. We investigated deconvolution artifacts and proposed a method to mitigate them via spatial regularisation.**

Our method was tested on Monte Carlo simulated data, using a water cylinder with aluminium inserts and two slices of an anthropomorphic phantom. Our results showed an improvement of spatial resolution in all cases (up to 29% or 60% for the cylindrical phantom, depending on whether deconvolution artifacts were corrected for or not). Overshoot artifacts were observed in the case of the cylindrical phantom but were less prominent in the case of the anthropomorphic phantom. In conclusion, we have shown that including the path uncertainty in the reconstruction can notably improve the spatial resolution.

***Index Terms*—deconvolution, deblurring, spatial resolution, proton CT, direct reconstruction**

I. Introduction

Proton computed tomography (pCT) has been investigated to complement or replace X-ray CT for proton treatment planning. While it offers a superior relative stopping power (RSP) accuracy compared to X-ray CT, it suffers from a lower spatial resolution. The spatial resolution of pCT is mainly impacted by multiple Coulomb scattering (MCS) of the protons and by the tracker resolution [1]. In list-mode pCT systems, front and rear trackers measure the position and direction of each proton upstream and downstream from the patient [2]. The most likely path (MLP) for each proton inside the patient, which can be computed using a compact formalism [3], is obtained from these measurements and has been shown to improve pCT reconstruction [4].

This work did not involve human subjects or animals in its research.

F. Khellaf was with University of Lyon, INSA-Lyon, Université Claude Bernard Lyon 1, UJM-Saint Etienne, CNRS, Inserm, CREATIS UMR 5220, U1206, F-69373, Lyon, France. She is now with Univ. Grenoble Alpes, CNRS, Grenoble INP, TIMC-IMAG, 38000 Grenoble, France.

N. Krah, J. M. Létang and S. Rit are with University of Lyon, INSA-Lyon, Université Claude Bernard Lyon 1, UJM-Saint Etienne, CNRS, Inserm, CREATIS UMR 5220, U1206, F-69373, Lyon, France.

N. Krah is also with Institut de Physique des Deux Infinis de Lyon, UMR 5822, F-69622, Villeurbanne, France.

The MLP itself has been included in both direct [5] and iterative reconstruction algorithms [6] to improve spatial resolution of pCT images. However, the uncertainty envelope around the MLP, which can also be calculated by the MLP formalism, has not yet been successfully used for reconstruction. Using the path uncertainty to improve spatial resolution has been mentioned in some works [3], [7]. Wang et al. [8] have tried to include this uncertainty in their projection matrix and performed reconstruction using an algebraic reconstruction technique (ART). However, their results did not show an improvement of spatial resolution compared to images reconstructed without using the path uncertainty. Unlike the method used in the aforementioned study, we propose to deconvolve pCT projections as an additional step in a direct reconstruction method, the distance-driven binning algorithm of Rit et al. [9]. The objective is to include the path uncertainty in the reconstruction to improve spatial resolution without compromising RSP accuracy. To estimate the path uncertainty in "realistic" conditions, we used an extended MLP formalism that takes into account the tracker's spatial and angular resolution (due to the strip pitch, scattering inside the tracker, etc.) [10].

Including the path uncertainty in the reconstruction is similar to resolution modeling in positron emission tomography (PET) imaging [11] where the resolution model is typically included in the system matrix and which has been shown to improve spatial resolution and contrast. It is known, however, that resolution modeling in PET may also lead to deconvolution artifacts, i.e. overshoots and ringing near edges [12]–[14], which can cause quantification errors [15]. Therefore, we investigated deconvolution artifacts in the context of pCT and proposed methods to control them.

Our deconvolution method was validated via Monte Carlo simulations in two phantoms: a water cylinder with aluminium inserts and an anthropomorphic phantom.

II. Materials and Methods

A. Distance-driven projection binning

The measured quantity in pCT is the proton's water equivalent path length (WEPL) which is the integral of the RSP along the proton path. In order to reconstruct pCT images, we first start by binning this list-mode data into projections. We apply the distance-driven binning procedure of Rit et al. [9] to take into account the non-linearity of the proton paths. The main idea is to bin the measured data along several virtual planes $k \in \{1, ..., K\}$ situated between the entrance and exit detectors according to the estimated MLP (Figure 1).

The coordinate system (u, v, w) is such that (u, v) define the detector plane, and w is taken along the main beam direction.

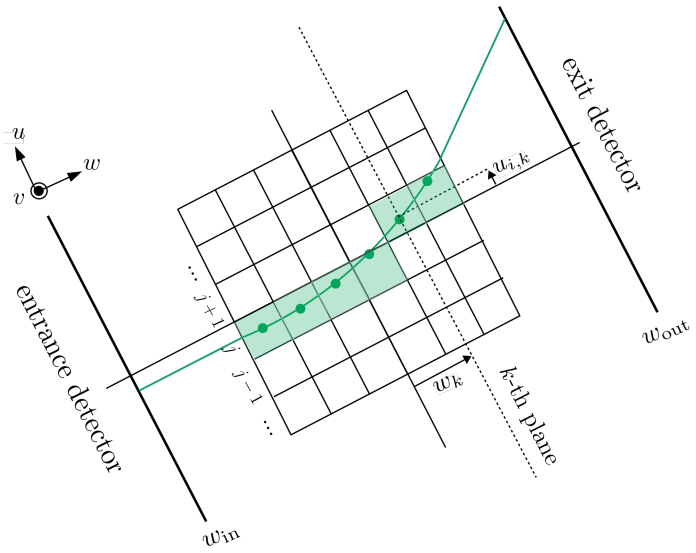

Fig. 1. Drawing of the coordinate system used for the distance-driven binning, for details see text.

The steps to compute the distance-driven projections are (i) to compute each proton's MLP and (ii) assign each proton's WEPL in the corresponding bin. More specifically, the MLP of the i-th proton is sampled at given distances w_k, with $k \in \{1, ..., K\}$, to have $u_{i,k}$ and $v_{i,k}$, the most likely position of the i-th proton in the k-th plane (Figure 1). The binned value in the j-th pixel of the k-th plane of the projection acquired with the p-th source position is

$$g_{j,k,p} = \frac{\sum_{i \in \mathbb{I}_p} \zeta_j(u_{i,k}, v_{i,k}, w_k) \text{WEPL}_i}{\sum_{i \in \mathbb{I}_p} \zeta_j(u_{i,k}, v_{i,k}, w_k)} \tag{1}$$

with $\mathbb{I}_p$ the subset of protons with source position p, ζ_j the indicator function for pixel j, and WEPL_i the water equivalent path length of proton i. The distance-driven projection can be interpreted as the backprojection of a single view p of the measured WEPL along the MLP. The rest of the reconstruction consists in filtering the sinogram with the usual ramp filter and doing a backprojection [9].

B. Path uncertainty

The proton path and the associated uncertainty can be computed using the MLP formalism [3]. The derivation assumes perfectly known entrance and exit positions and angles per proton $\mathbf{y}_{\text{in}} = (u_{\text{in}}, \theta_{\text{in}})$ and $\mathbf{y}_{\text{out}} = (u_{\text{out}}, \theta_{\text{out}})$, measured at distances w_{in} and w_{out} (Figure 1). In practice, the spatial and angular resolution of the trackers will induce an uncertainty on the measured parameters. Krah et al. [10] have included the impact of detector resolution in the MLP formalism. We briefly recall their formalism and give the formulas used to compute the uncertainty envelope.

First, the joint probability that a proton passes through $\mathbf{y}_1$, an intermediary vector inside the object, and $\tilde{\mathbf{y}}_{\text{out}}$ given $\tilde{\mathbf{y}}_{\text{in}}$ (tilde distinguishes measured from true vectors) is redefined as

$$\begin{aligned} L(\mathbf{y}_1, \tilde{\mathbf{y}}_{\text{out}} | \tilde{\mathbf{y}}_{\text{in}}) = &\int L_{\text{scat}}(\mathbf{y}_1 | \mathbf{y}_{\text{in}}) L_{\text{meas}}(\tilde{\mathbf{y}}_{\text{in}} | \mathbf{y}_{\text{in}}) \, \mathrm{d}\mathbf{y}_{\text{in}} \\ &\times \int L_{\text{scat}}(\mathbf{y}_{\text{out}} | \mathbf{y}_1) L_{\text{meas}}(\tilde{\mathbf{y}}_{\text{out}} | \mathbf{y}_{\text{out}}) \, \mathrm{d}\mathbf{y}_{\text{out}} \end{aligned} \tag{2}$$

where $L_{\text{scat}}(\mathbf{y}_1 | \mathbf{y}_{\text{in}})$ and $L_{\text{scat}}(\mathbf{y}_{\text{out}} | \mathbf{y}_1)$ represent the likelihoods that a proton is scattered from $\mathbf{y}_{\text{in}}$ to $\mathbf{y}_1$, and from $\mathbf{y}_1$ to $\mathbf{y}_{\text{out}}$, respectively; and $L_{\text{meas}}(\tilde{\mathbf{y}}_{\text{in}} | \mathbf{y}_{\text{in}})$ and $L_{\text{meas}}(\tilde{\mathbf{y}}_{\text{out}} | \mathbf{y}_{\text{out}})$ represent the likelihoods of the measured values $\tilde{\mathbf{y}}_{\text{in}}$ and $\tilde{\mathbf{y}}_{\text{out}}$ to be the true parameters $\mathbf{y}_{\text{in}}$ and $\mathbf{y}_{\text{out}}$, respectively. The probabilities L_{meas} are modeled with a Gaussian distribution as it describes well the statistical error in experiments. Solving the integrals in Equation 2 and reshaping into Gaussian functions gives an expression for the MLP and an uncertainty matrix that takes into account measurement uncertainties. The corresponding error matrix is given by [10]

$$\mathbf{\Sigma}_{\text{MLP}}(w) = \mathbf{C}_1 (\mathbf{C}_1 + \mathbf{C}_2)^{-1} \mathbf{C}_2 \tag{3}$$

with

$$\mathbf{C}_1 = \mathbf{R}_0 \mathbf{S}_{\text{in}} \mathbf{\Sigma}_{\text{in}} \mathbf{S}_{\text{in}}^T \mathbf{R}_0^T + \mathbf{\Sigma}_1 \tag{4}$$

$$\mathbf{C}_2 = \mathbf{R}_1^{-1} \mathbf{S}_{\text{out}}^{-1} \mathbf{\Sigma}_{\text{out}} (\mathbf{S}_{\text{out}}^{-1})^T (\mathbf{R}_1^{-1})^T + \mathbf{R}_1^{-1} \mathbf{\Sigma}_2 (\mathbf{R}_1^{-1})^T. \tag{5}$$

The uncertainty on the path position relative to the MLP $\sigma_{\text{MLP}}(w) = \mathbf{\Sigma}_{\text{MLP}}(w)_{1,1}$ is given by the element in the first row and first column of $\mathbf{\Sigma}_{\text{MLP}}$. The expressions for rotation matrices $\mathbf{R}_0, \mathbf{R}_1$ and scattering matrices $\mathbf{\Sigma}_1, \mathbf{\Sigma}_2$ are the ones used in the usual MLP formalism [3]. The matrices $\mathbf{S}_{\text{in}}$ and $\mathbf{S}_{\text{out}}$ propagate the measured positions from the detector to the object surface

$$\mathbf{S}_{\text{in}} = \begin{pmatrix} 1 & d_{\text{entry}} \\ 0 & 1 \end{pmatrix}, \; \mathbf{S}_{\text{out}} = \begin{pmatrix} 1 & d_{\text{exit}} \\ 0 & 1 \end{pmatrix}, \tag{6}$$

with d_{entry} the distance from the front tracker to the entrance position and d_{exit} the distance from the rear tracker to the exit position. The matrices $\mathbf{\Sigma}_{\text{in}}$ and $\mathbf{\Sigma}_{\text{out}}$ describe uncertainties due to the trackers' finite spatial and angular resolution. They are given by the sum of the uncertainty due to the spatial resolution of the trackers σ_t and the error due to scattering inside the trackers

$$\mathbf{\Sigma}_{\text{in}} = \sigma_t^2 \mathbf{T}_{\text{in}} \mathbf{T}_{\text{in}}^T + \mathbf{\Sigma}_{\text{sc,in}} \tag{7}$$

$$\mathbf{\Sigma}_{\text{out}} = \sigma_t^2 \mathbf{T}_{\text{out}} \mathbf{T}_{\text{out}}^T + \mathbf{\Sigma}_{\text{sc,out}} \tag{8}$$

where $\mathbf{T}_{\text{in}}$ and $\mathbf{T}_{\text{out}}$ are the matrices relating the positions measured by the two detectors in each pair to the position/direction parameters:

$$\mathbf{T}_{\text{in}} = \begin{pmatrix} 0 & 1 \\ -1/d_T & 1/d_T \end{pmatrix}, \mathbf{T}_{\text{out}} = \begin{pmatrix} 1 & 0 \\ -1/d_T & 1/d_T \end{pmatrix}, \tag{9}$$

with d_T the distance between the trackers. Finally, the matrices $\mathbf{\Sigma}_{\text{sc,in}}$ and $\mathbf{\Sigma}_{\text{sc,out}}$ represent the impact of the scattering inside the trackers on the angular uncertainty

$$\mathbf{\Sigma}_{\text{sc,in}} = \begin{pmatrix} 0 & 0 \\ 0 & \sigma_{\text{sc,in}}^2 \end{pmatrix}, \mathbf{\Sigma}_{\text{sc,out}} = \begin{pmatrix} 0 & 0 \\ 0 & \sigma_{\text{sc,out}}^2 \end{pmatrix}, \tag{10}$$

with

$$\sigma^2_{\text{sc,in}} = \frac{E_0^2}{p^2(E_{\text{in}})v^2(E_{\text{in}})}\frac{x}{X_0}\Big(1+0.038\ln\frac{x}{X_0}\Big)^2, \quad (11)$$

$$\sigma^2_{\text{sc,out}} = \frac{E_0^2}{p^2(E_{\text{out}})v^2(E_{\text{out}})}\frac{x}{X_0}\Big(1+0.038\ln\frac{x}{X_0}\Big)^2, \quad (12)$$

where $E_0 = 13.6$ MeV and 0.038 are empirical constants, x/X_0 represents the material budget, i.e. the ratio between the tracker thickness and the radiation length of the tracker material (silicon), and the term $1/p^2(E)v^2(E)$ is approximated using a 5$^{\text{th}}$-degree polynomial [3].

Equation 3 computes the path uncertainty envelope for each proton. In order to use this information to deblur the binned distance-driven projections, we perform a distance-driven binning of the path uncertainty similarly to Equation 1:

$$\sigma_{j,k,p} = \sqrt{\frac{\sum_{i\in\mathbb{I}_p}\zeta_j(u_{i,k},v_{i,k},w_k)\sigma^2_{\text{MLP},i}(w_k)}{\sum_{i\in\mathbb{I}_p}\zeta_j(u_{i,k},v_{i,k},w_k)}} \quad (13)$$

with $\sigma^2_{\text{MLP},i}(w_k)$ the variance of the path of proton i relative to its MLP at distance w_k. The value $\sigma_{j,k,p}$ represents the average standard deviation of the paths of protons emitted from the p-th source position passing in the j-th pixel and the k-th plane relative to their MLPs.

C. Spatially variant blurring model

As the blur occurs in the (u,v) plane of the binned projections $g_{j,k,p}$, we consider each plane k of the distance-driven projections individually. Although the blur in a real pCT projection is the result of vertical and lateral components, we do not consider the blur in the v-direction in our approach. We work with one-line projections of a 3D image, which limits our problem to a set of 1D deconvolutions as modeled below, and leave 2D deconvolution of 2D projections to future work.

If the blur were spatially invariant, the measured projection would be the result of the convolution of an ideal projection $g^*_{j,k,p}$ with a shift-invariant convolution kernel. As the blur depends on the position u, which is referred to by the 1D pixel index j, we model the measured projection as the result of a shift-variant operation

$$g_{j,k,p} = \sum_m h_{j-m,m,k,p}\,g^*_{m,k,p} \quad (14)$$

where $h_{j-m,m,k,p}$ is computed from a Gaussian function due to the Gaussian model used for the path uncertainty

$$h_{j-m,m,k,p} = \frac{1}{\sqrt{2\pi}\sigma_{m,k,p}}\exp\Big(-\frac{(j-m)^2\tau^2}{2\sigma^2_{m,k,p}}\Big), \quad (15)$$

with τ the projection spacing and $\sigma_{m,k,p}$ the path uncertainty, both in millimeters. In matrix notation, Equation 14 becomes

$$\mathbf{g}_{k,p} = \mathbf{H}_{k,p}\mathbf{g}^*_{k,p} \quad (16)$$

where $\mathbf{g}_{k,p}$ is a vector containing one line of the distance-driven projection, $\mathbf{H}_{k,p}$ is the shift-variant system matrix, and $\mathbf{g}^*_{k,p}$ is a vector containing one line of the projection without blurring.

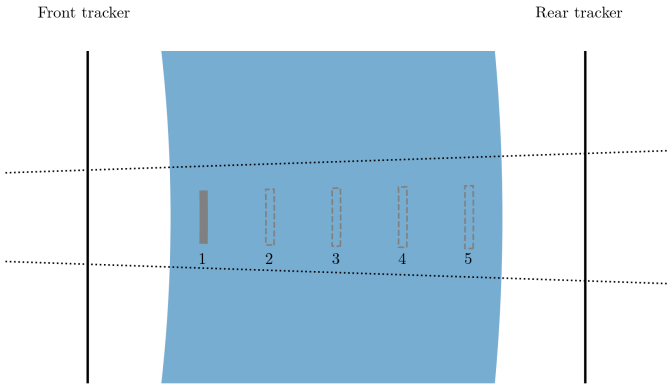

Fig. 2. Setup of the five simulations with a bone insert in water. Only one insert was modeled per simulation. The position of the insert for simulations 1 to 5 is shown. The inserts and the water shell have the same curvature.

The formalism presented in Section II-B provides an estimate of the path uncertainty due to multiple Coulomb scattering and tracker resolution. Using a phantom with three inserts at different depths, it has been shown that the best resolution for each insert is obtained at the distance corresponding to the depth of the insert [9]. At other distances, the non-linearity of the proton paths causes further blurring. In the final image, the distances contributing to reconstructing the inserts are those corresponding to their depths. Therefore, we neglect this effect and consider that modeling the blurring in the projections using the path uncertainty is sufficient. This assumption will be verified using a phantom with inserts at different depths.

D. Deconvolution method

In practice, due to the presence of noise, the true solution of an inverse problem such as the one in Equation 16, even if well-posed, cannot be found exactly. Approximate solutions can be obtained using, for example, a least squares estimate

$$\hat{\mathbf{g}}_{k,p} = \arg\min_{\mathbf{g}^*_{k,p}} ||\mathbf{H}_{k,p}\mathbf{g}^*_{k,p} - \mathbf{g}_{k,p}||_2^2. \quad (17)$$

However, the unregularized deconvolution problem does not necessarily have a unique solution [14]. In practice, this means it is impossible to recover high frequency components that could not be measured by the system due to its spatial resolution. Any values assigned to these high frequency components produce a different possible solution. Specifically, the overshoot artifacts usually observed in deconvolution problems correspond to the sharp frequency cut-off between the restored frequencies and the high frequencies set to zero. A regularization term is therefore necessary to constrain the problem, which becomes

$$\hat{\mathbf{g}}_{k,p} = \arg\min_{\mathbf{g}^*_{k,p}} ||\mathbf{H}_{k,p}\mathbf{g}^*_{k,p} - \mathbf{g}_{k,p}||_2^2 + \alpha^2||\nabla\mathbf{g}^*_{k,p}||_2^2 \quad (18)$$

with α the regularization parameter. Regularization helps to attenuate overshoot artifacts by imposing a smoother cut-off between low and high frequencies, but it does not completely suppress them, as our results will confirm.

These artifacts causing overshoots near edges have been observed in resolution modeling for emission reconstruction [12]–[14]. Note that they persist even with perfect knowledge of the system matrix. A relationship between the amplitude of those artifacts and the imaging matrix which maps the object to the projection space has been established [12]. As the point spread function (PSF) gets wider, the matrix rank gets lower (i.e. the problem is more underdetermined) and its condition number higher, which produces worse artifacts. Different methods have been proposed to deal with this problem in the context of PET imaging, e.g. post-smoothing the image or using different regularization procedures. But they are not all directly applicable to our problem since the resolution model is included in the system matrix in PSF-based PET reconstruction, which is not the case in our framework. We have selected one method, tested in different papers [12], [13], which consists in underestimating the PSF. As the artifacts appear with high uncertainty values, underestimating those values will reduce the overshoots observed on deblurred images, although this will limit the improvement of the spatial resolution. In practice, this uncertainty underestimation can be interpreted as the reconstruction of an image acquired with better detectors and lower MCS rather than ideal detectors and no MCS. We denote our underestimated system matrix by $\mathbf{H}^{\beta}_{k,p}$ corresponding to the following kernel

$$h_{j-m,m,k,p} = \frac{1}{\sqrt{2\pi}\beta\sigma_{m,k,p}} \exp\Big(-\frac{(j-m)^2\tau^2}{2\beta^2\sigma^2_{m,k,p}}\Big) \quad (19)$$

where $\beta \in (0,1]$ represents the uncertainty underestimation factor. Setting β to 1 corresponds to the use of the exact path uncertainty. Using the scaled system matrix, we take the regularized least squares solution

$$\hat{\mathbf{g}}_{k,p} = \arg\min_{\mathbf{g}^*_{k,p}} \; ||\mathbf{H}^{\beta}_{k,p}\mathbf{g}^*_{k,p} - \mathbf{g}_{k,p}||^2_2 + \alpha^2||\nabla\mathbf{g}^*_{k,p}||^2_2. \quad (20)$$

This problem was solved using a conjugate gradient method, for all planes k and all projections p before reconstruction. The scaling and regularization parameters α and β were chosen to have a good trade-off between spatial resolution and overshoot as described in the next section.

E. Simulations

The first simulations, performed using GATE [16] version 9.0 with the QGSP_BIC physics list, were used to validate our blurring model. The simulations are similar to the one performed by Rit et al. [9]. In each simulation, we acquired a single projection of a 20 cm wide shell of water with a 5 mm wide bone insert (Figure 2). Five different simulations were acquired for five positions of the insert (one insert per simulation). Since a fan beam was used, we made the water shell and the inserts truncated hollow spheres with the same origin as the beam, such that the ideal projection (if no MCS was involved) would be a rectangular function. The internal and external radii were 100±10 cm for the water shell, and 92±0.25, 96±0.25, 100±0.25, 104±0.25, and 108±0.25 for the inserts. The inserts were truncated using an angular span of 2 degrees. The beam energy was 200 MeV and the fluence at the isocenter was about 2×10^5 protons·mm^{-2}. The spatial resolution in the projection, as a function of depth, was compared to the predicted resolution using the path uncertainty. The spatial resolution was measured by fitting an error function to the edges of the projection of the inserts, similarly to [5]. More specifically, for each insert, and for each distance w in the projection of the insert, the following function

$$\frac{A}{2}\Big(1 + \mathrm{erf}\Big(\frac{x-\mu}{\sigma\sqrt{2}}\Big)\Big) + B \quad (21)$$

was fitted to the projection data as illustrated in Figure 5a. The fitted parameter σ was used as a measure for the spatial resolution.

Other simulations were made to evaluate the capability of the proposed deconvolution method to improve spatial resolution. We used the same simulation for the spiral phantom as the one described in a previous study [9], except that the radius of the aluminium beads was increased from 5 to 10 mm. A 200 MeV fan beam with a fluence of 225 protons·mm^{-2}·projection^{-1} at the isocenter was simulated. The spiral phantom was also used to choose the scaling and regularization parameters α and β. In addition, we simulated an acquisition using the ICRP female phantom [17]. A uniform 250 MeV beam energy was used to traverse the phantom volume everywhere (note that a variable energy could

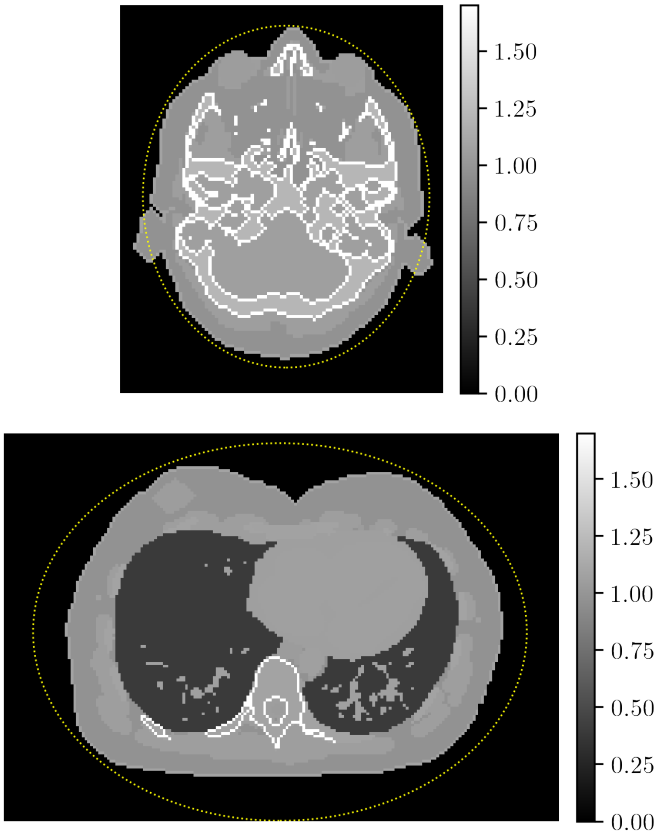

Fig. 3. Reference RSP maps of the reconstructed slices. The dotted yellow lines represent the hulls used to compute the MLP.

have been used depending on the scanned slice), with a flux of 190 protons·mm^{-2}·projection^{-1}. In all our simulations, a high number of protons was simulated in order to have low noise and thus a good measure of spatial resolution. A total of 720 projections over 360° were simulated. Two slices, one through the posterior fossa and the other through the heart, were reconstructed (Figure 3). To compute the MLP and the path uncertainty, the convex hull of the spiral phantom was known and that of the head and lung slices of the ICRP phantom was approximated by an ellipse for fast detection of the intersection between the patient and the proton path before and after the patient. The sampling for the distance-driven projections was 0.625×0.625 mm^2 for all phantoms. The spiral phantom was reconstructed on a grid of 0.5×0.5 mm^2 pixels, and the ICRP phantoms on a grid of 1.775×1.775 mm^2 pixels – the same sampling as the reference phantoms.

The GATE simulation was performed using an idealized setup, i.e. with error-less position and angle measurements. Tracker uncertainties were included by postprocessing the output of the simulation. Specifically, for each proton, a Gaussian error with a covariance given by Equations 7 and 8 is added to the ideal entrance/exit parameters. To compute the covariance matrices, we used a spatial resolution of $\sigma_t = 0.066$ mm corresponding to a strip pitch of 228 µm, a material budget of $x/X_0 = 5 \times 10^{-3}$ and a distance $d_T = 10$ cm between the trackers in each pair. These values meet or exceed the minimum specifications for pCT scanner prototypes as detailed in [18]. The closest trackers of each pair were placed at a distance of 40 cm from the isocenter, which corresponds to distances used in commercial X-ray CT scanners [10]. Images were reconstructed from data without and with tracker uncertainties using the standard MLP formalism [3] and the extended one [10], respectively, to compute the proton path and the uncertainty maps. Spatial resolution was calculated in the spiral phantom corresponding to an MTF value of 10% using the approximate method described in [5] based on [19]. The function given in Equation 21 was fitted to each bead's radial profile (see Figure 4 for an example of a radial profile), and the MTF10% was derived as

$$\mathrm{MTF10\%} = \sqrt{\frac{\ln 10}{2}}\frac{1}{\pi\sigma}. \tag{22}$$

In order to choose the scaling and regularization parameters, the spiral phantom was reconstructed using values of β ranging from 0.5 to 1 at intervals of 0.1, and values of α ranging from 0.05 to 0.9 at intervals of 0.05. The average spatial resolution and average overshoot over all beads were measured for each reconstruction, and the pair of parameters giving the best resolution/overshoot trade-off was chosen and applied to the anthropomorphic phantoms. The overshoot in each bead was measured by taking the radial profile (as for the spatial resolution), and computing the relative difference between the maximum value and the true RSP value of the beads (RSP = 2.1), after post-smoothing the profile with a Gaussian kernel of standard deviation 0.1 mm and width 8 mm (equal to the size of the profile) to reduce noise (Figure 4). Negative overshoot values occurred when there were no oscillations and the edges remained blurred due to loss of spatial resolution.

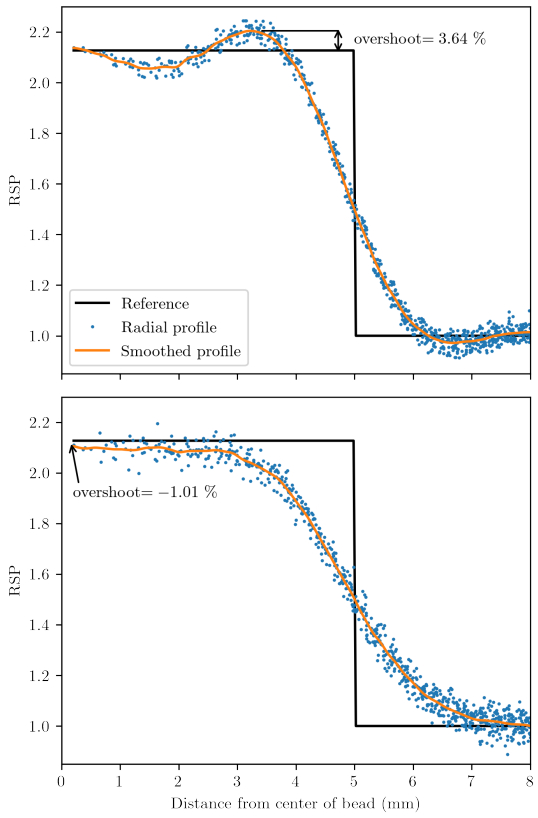

Fig. 4. Example profiles of inserts in the spiral phantom used to measure the overshoot. The top profile is from a deblurred image without underestimation, and the bottom one from a non-deblurred image, hence the negative "overshoot".

III. RESULTS

A. Resolution modeling and uncertainty maps

Figure 5b shows the spatial resolution measured in the five distance-driven projections of the inserts positioned as depicted in Figure 2, acquired using either ideal or realistic trackers. The spatial resolution was measured as explained in Section II-E, i.e. by fitting Equation 21 to the edge spread function of each insert and for each distance w. The theoretical path uncertainty shows a good agreement with the spatial resolution measured in the projections at the depths corresponding to the insert positions. At other depths, the path uncertainty does not reflect the spatial resolution due to the non-linearity of the proton path, as discussed in Section II-C. The dashed line shows the effect of pixel size (0.5 mm) on the overall uncertainty. The added uncertainty was taken into account by computing the quadratic sum $\sigma^2_{\mathrm{total}} = \sigma^2_{\mathrm{MLP}} + \sigma^2_{\mathrm{pixel}}$, with $\sigma_{\mathrm{pixel}} = 0.5/\sqrt{12}$ and σ_{MLP} as defined in Equation 3. It is overall non negligible close to the entrance and exit of the phantom in the case of ideal trackers, while it is negligible in the case of realistic trackers because the path uncertainty dominates the loss of spatial resolution.

Figure 6 shows path uncertainty maps for the spiral phantom, with and without tracker uncertainties. For the case without tracker uncertainty, there is no variability as a function of the projection angle due to the fact that the object is

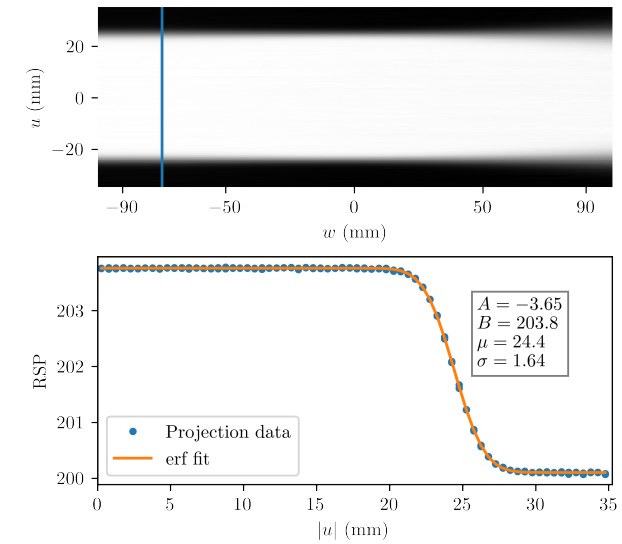

(a)

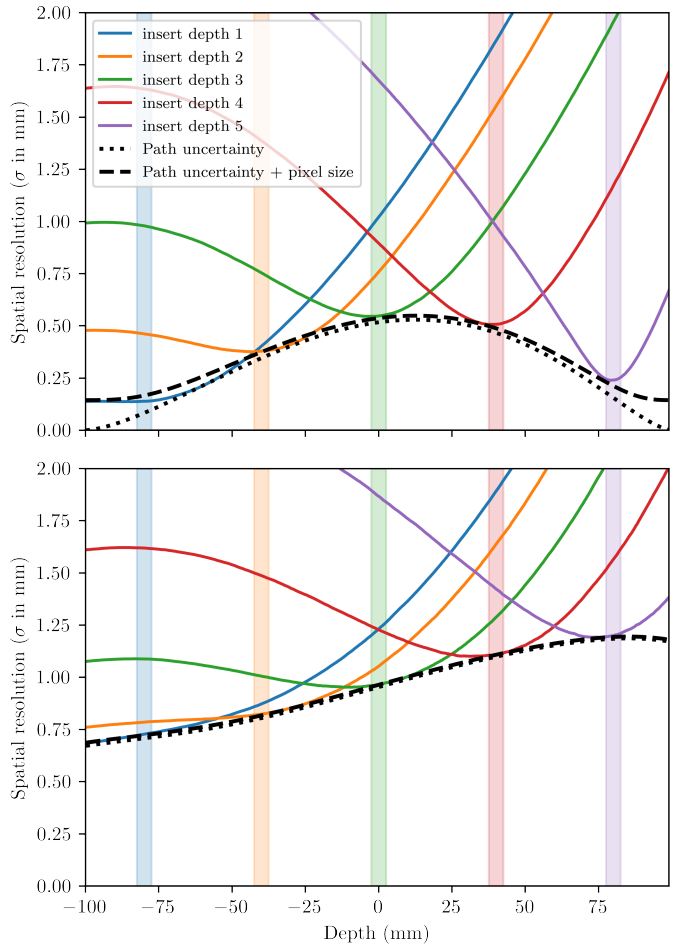

(b)

Fig. 5. (a) Distance-driven projection for insert position 3 (see Figure 2). One line of the projection (indicated by the blue vertical line) is plotted against the absolute position $|u|$, and the erf fit is used to compute the spatial resolution σ. The fit parameters of Equation 21 are given in the text box. (b) Spatial resolution as a function of depth measured on the projections corresponding to each insert position, compared with the path uncertainty, for ideal trackers (top) and realistic trackers (bottom). The vertical bars indicate the depth of the insert in colors corresponding to the curves.

circular. The uncertainty due to MCS reaches a maximum of about 0.5 mm approximately at the center of the object. The maximum is not exactly at the central depth due to the energy loss term in the computation of the scattering matrices $\mathbf{\Sigma}_1, \mathbf{\Sigma}_2$. It is slightly shifted towards the exit of the proton path. Adding tracker uncertainties increases the maximum uncertainty value to about 1.4 mm and shifts it towards the exit. We further observe high uncertainty streaks near the exit of the path of the protons, corresponding to protons traversing aluminium inserts and losing more energy than those traversing fewer or no inserts. Those lower energy protons scatter more in the rear tracker (see energy term in Equation 12), hence a higher uncertainty.

Figure 7 shows uncertainty maps for the lung and head phantoms for two different source positions, with and without tracker resolution. There is a larger variability of the uncertainty values between different projections compared to the maps of the spiral phantom. This is due to the elliptical shapes of the convex hulls used to approximate the phantom surface. This inter-projection variability is more pronounced for the lung phantom, with a maximum path uncertainty in the first projection (traversing the left-right axis of the patient) of 1.7/1.8 mm with/without tracker resolution, and a maximum for the second projection (traversing the antero-posterior axis of the patient) of 0.8/1 mm. Spatial variability due to RSP heterogeneities is visible in both phantoms when using realistic trackers. For example, in the lung phantom, trajectories traversing the lung tissues are associated with a lower uncertainty (visible near the exit of the phantom).

B. Spiral phantom and choice of scaling and regularization parameters

Figure 8 shows the quantification of the overshoot (see Section II-E) as a function of spatial resolution for different scaling and regularization parameters. Each data point represents the average overshoot and spatial resolution (averaged over all inserts) in the spiral phantom reconstructed with a different pair of (α, β) parameters. The goal was to find the pair (α, β) which yields about zero overshoot and the highest possible resolution. In terms of the figures, we seek the rightmost data point on the dotted line corresponding to an overshoot of zero. With ideal trackers, such a point can be found with $\beta = 1$, i.e. without underestimation of the uncertainty. With realistic trackers, setting $\beta = 0.7$ gave the highest resolution for an overshoot very close to zero (given the tested β values, the actual optimal parameter is somewhere between 0.7 and 0.8).

Representative reconstructions of the spiral phantom, used to plot Figure 8, are shown in Figure 9. The deblurred results with ($\beta = 0.7$) and without ($\beta = 1$) uncertainty underestimation are shown for a regularization of $\alpha = 0.2$. Overshoots appear as ring-like structures, as in the lower central panel. The reconstructions are consistent with the measured overshoots in Figure 8: no artifact is visible in the images acquired with ideal trackers, while the reconstruction from realistic trackers without underestimation shows an overshoot which is corrected when using $\beta = 0.7$. The corresponding

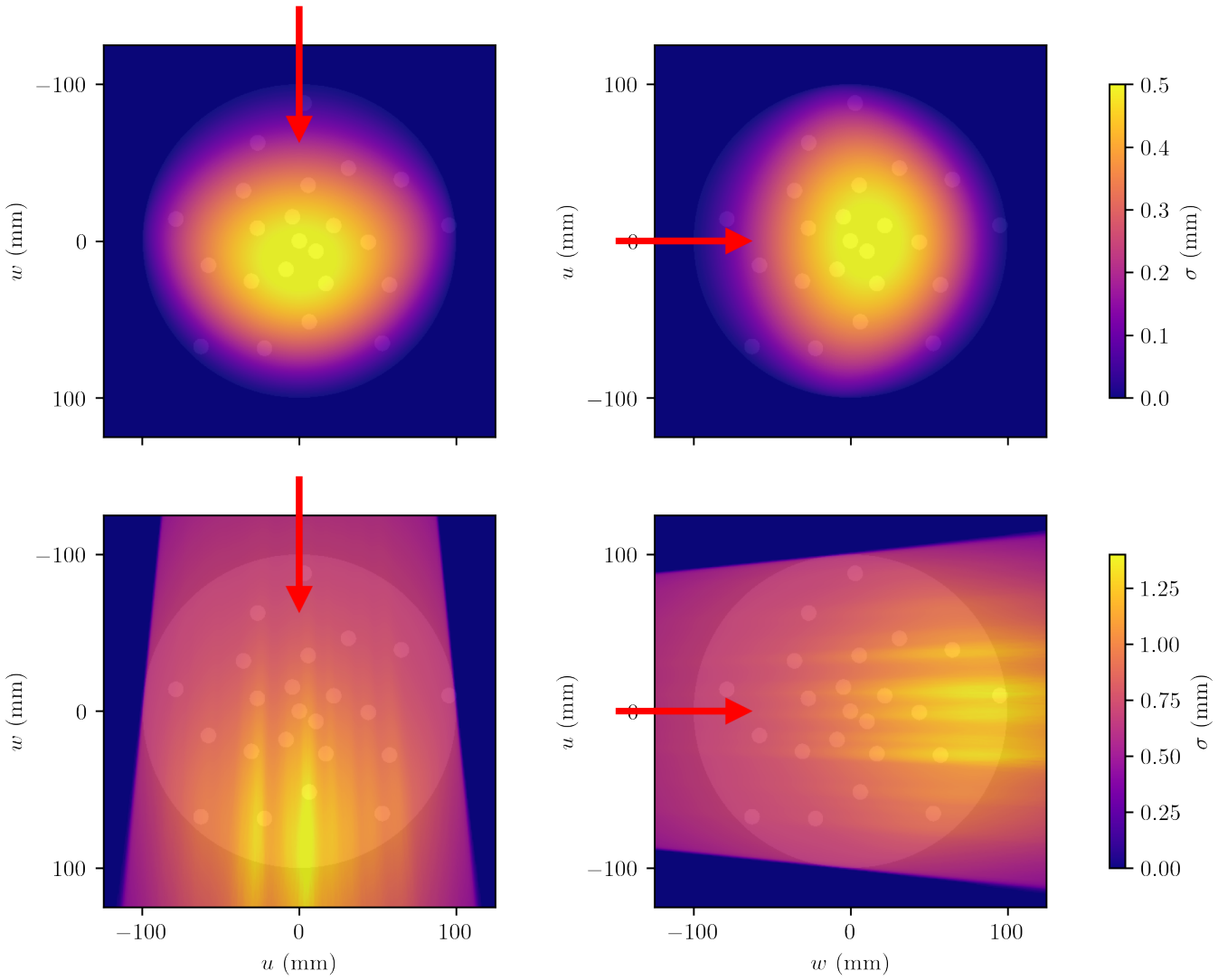

Fig. 6. Uncertainty maps of the spiral phantom introduced by an ideal tracker (top) or a realistic tracker (bottom) for two different source positions (the beam directions are indicated by red arrows). The phantom geometry is depicted with low opacity in a different color map for better visualization.

spatial resolutions are plotted in Figure 10 as a function of distance from the phantom center. For ideal trackers, there is an improvement of the spatial resolution for the central beads, up to 28% without overshoot correction and up to 11% with overshoot correction. For beads that are far away from the center, the spatial resolution is reduced due to the regularization. For realistic trackers, the spatial resolution is improved for all beads. The gain of resolution is up to 29% with overshoot correction and up to 60% without correction.

C. Anthropomorphic phantoms

The reconstructions for the head and lung phantoms using realistic trackers are shown in Figure 11. The difference maps indicate the improvement in spatial resolution along anatomical edges. Overall, the deblurred reconstructions show a better spatial resolution. For the head phantom, the error is more reduced without underestimation of the uncertainty ($\beta = 1$); while for the lung phantom, the error near anatomical edges is smaller with a scaling factor $\beta = 0.7$. This is reflected by the root mean square error (RMSE) measured inside the zoomed regions-of-interest. For reconstructions using ideal trackers, no improvement was seen.

IV. DISCUSSION

The purpose of this work was to investigate the use of the path uncertainty to improve spatial resolution in proton CT images. First, we verified that the path uncertainty is an accurate measure for the spatial resolution in the projections at the distance corresponding to the position of the edge in the object (Figure 5). Second, we generated distance-driven uncertainty maps corresponding to the pCT projections. As the estimated path uncertainty depends on the shape of the object to be imaged and on the heterogeneities inside the object (in the case of realistic trackers), the values in the maps vary as a function of the projection angle, the depth and the transverse position. Specifically, the less circular the object, the more the uncertainty values vary between different

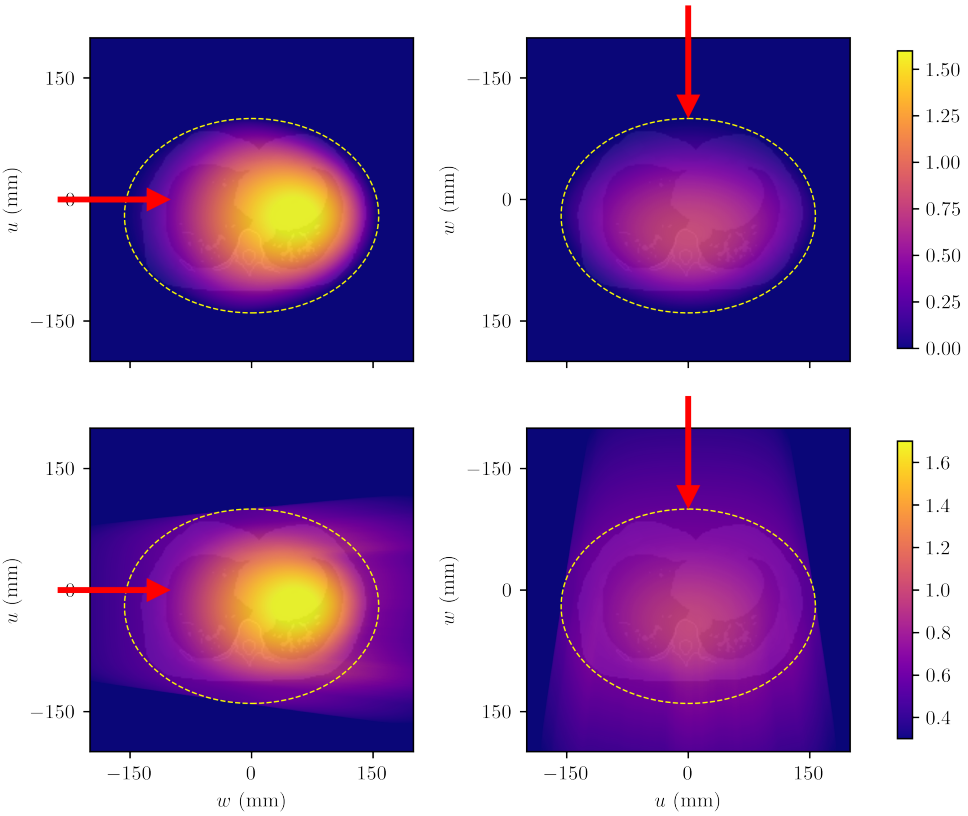

(a) Lung

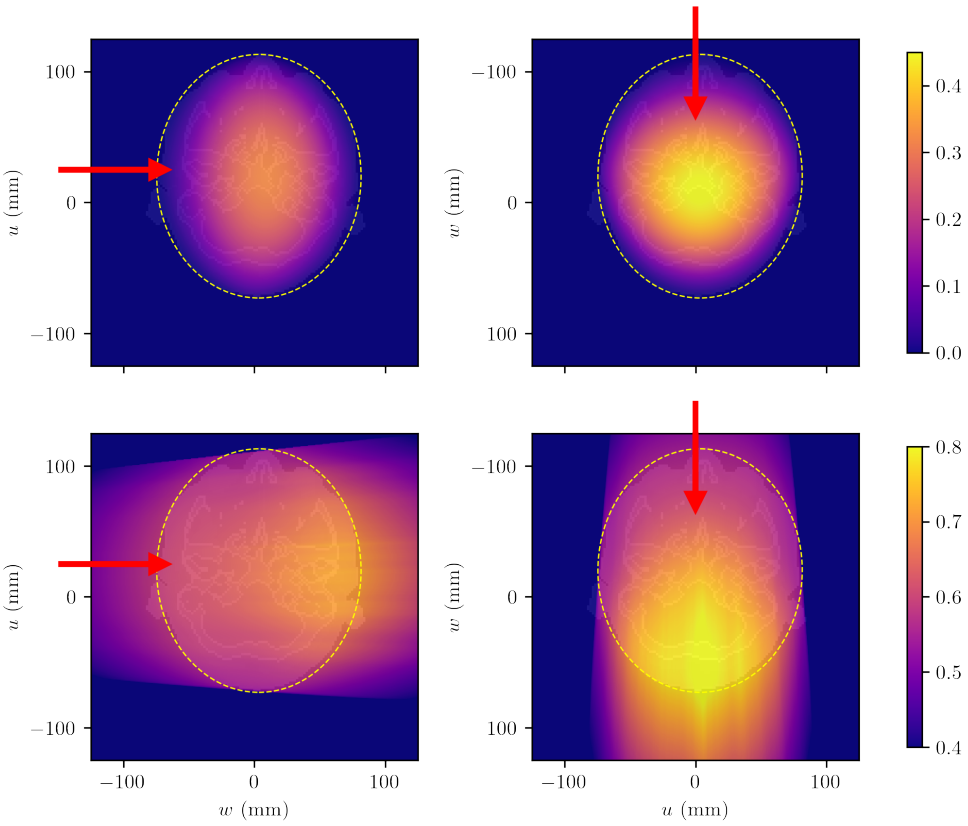

(b) Head

Fig. 7. Uncertainty maps without tracker resolution (first and third rows) and with tracker resolution (second and fourth rows) for two different source positions (the beams directions are indicated by red arrows). The ellipse used to approximate the phantom surface is shown with a yellow dashed line.

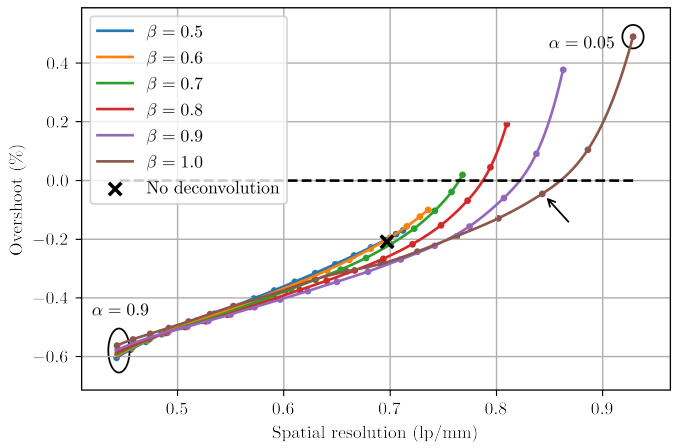

(a) Ideal trackers

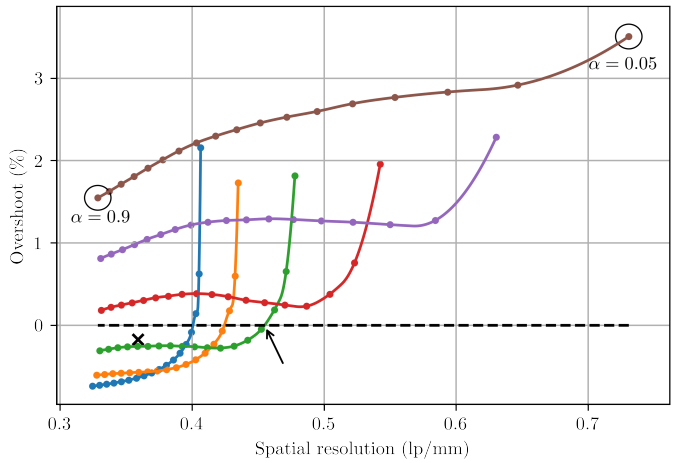

(b) Realistic trackers

Fig. 8. Overshoot vs spatial resolution in the spiral phantom for ideal trackers (top) and realistic trackers (bottom). Each curve is computed for a different β parameter. The regularization parameter α, corresponding to the different data points for each curve, ranges between 0.05 and 0.9 in steps of 0.05 (low values of α lead to high resolution and vice versa as shown by the two circled data points). The arrows point to the tested (α, β) parameters giving the highest spatial resolution for an overshoot close to zero.

projections. For example, there was about a factor 2 between the maximum uncertainty for protons traversing the large and short axes of the lung phantom (Figure 7). Including tracker resolution in the MLP model increased the path uncertainty compared with ideal trackers, where only MCS in the object is relevant. Although both the standard and the extended MLP formalism assume a homogeneous medium, the impact of heterogeneities inside the phantom on the path uncertainty was partially taken into account through the energy term used for the computation of the scattering inside the rear detector ($p^2(E_{\text{out}})v^2(E_{\text{out}})$ term in Equation 12). For example, protons that traversed aluminium inserts in the spiral phantom had lower exit energies and scattered more in the rear tracker than protons that traversed no inserts, and therefore led to higher MLP uncertainties along projection lines crossing the inserts (Figure 6). Conversely, protons that traversed air in the lung phantom led to lower MLP uncertainties.

Using the computed uncertainty maps to deconvolve the pCT projections, we observed overshoots near edges in the deblurred reconstructions. Those are common side effects to deconvolution [12]–[14]. The RSP accuracy of the deblurred image can be compromised by such artifacts: in order to limit this effect to an acceptable level, stringent requirements must be set (our objective is to have an average overshoot close to zero). We studied the effect of overshoots in the spiral phantom (Figure 8). In the ideal case, as the uncertainty values are smaller, the average overshoot was small (maximum measured average overshoot of less than 0.5% in the spiral phantom). However, with realistic trackers, the average overshoot could exceed 3% and was not effectively suppressed by the regularization term alone. Indeed, using either the regularization or the β parameter alone was not sufficient to reduce the average overshoot to zero: in Figure 8, the line corresponding to $\beta = 1$ is well above the zero average overshoot line regardless of the regularization; similarly, very small regularizations ($\alpha = 0.05$) led to high average overshoots regardless of the β parameter. In addition, using both strategies allows for a better trade-off between overshoot and spatial resolution. Increasing the regularization factor α alone managed to reduce the average overshoot, but at the cost of a considerable loss of spatial resolution: for example, without underestimation, reducing the average overshoot below 2% required a regularization of at least $\alpha = 0.7$ which led to a resolution of 0.37 lp/mm. In contrast, underestimating the uncertainty by 10% ($\beta = 0.9$) managed to reduce the average overshoot well below 2% with $\alpha = 0.1$ and a resolution of 0.58 lp/mm. Therefore, combining both methods was necessary to produce an overshoot-free image with a high spatial resolution. In this work, we chose the β value which corresponded to an average overshoot of zero and a high resolution, as our objective was to improve spatial resolution without compromising the image quality by introducing overshoot artifacts. However, depending on the specific application, if a certain amount of artifacts is acceptable in the image, further improvement of the spatial resolution is possible by using a larger β parameter. Indeed, overshoots are object dependent: regularly shaped objects such as cylinders lead to characteristic artifacts, e.g. rings; while in less regularly structured objects, overshoot artifacts might appear more like noise.

The reconstructed images of the spiral phantom using realistic trackers showed an increase of spatial resolution between 22% and 29% when an underestimation of the uncertainty was included and between 49% and 60% without underestimation (Figure 10). The gain of spatial resolution was largest at the center of the object where spatial resolution is the lowest. The results with ideal trackers for the spiral phantom showed an improvement of spatial resolution only at the center of the object. At the surface, the resolution was not enhanced as the path uncertainty was already close to zero. In fact, the spatial resolution was even slightly reduced, depending on the value of the regularization parameter α. In this work, α was empirically chosen based on average measurements over different locations in the phantom. In principle, α could be spatially variant as less regularization is needed at the surface. In practice, i.e. with realistic trackers, path uncertainty within

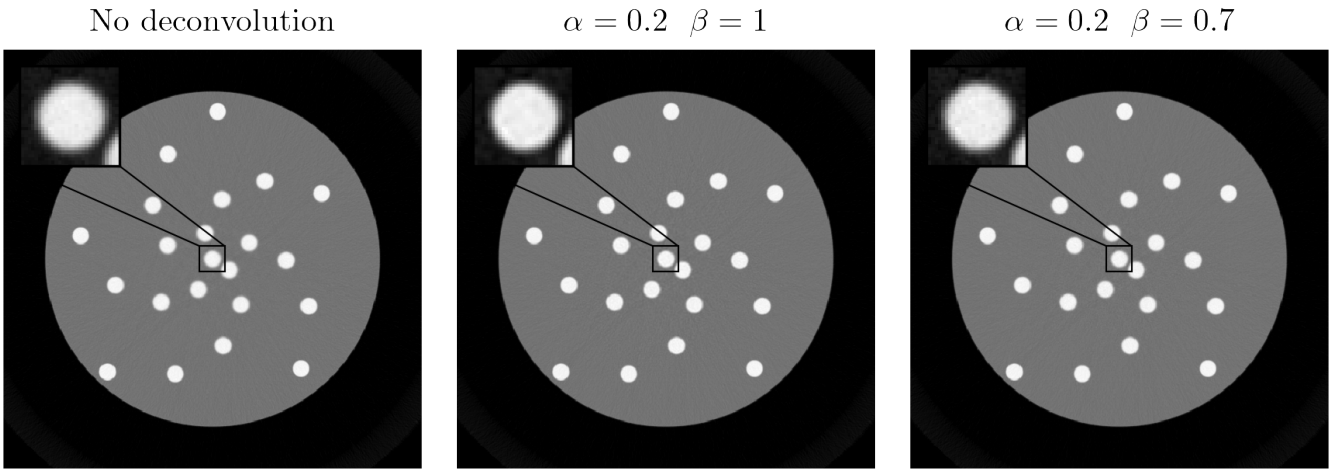

(a) Ideal trackers

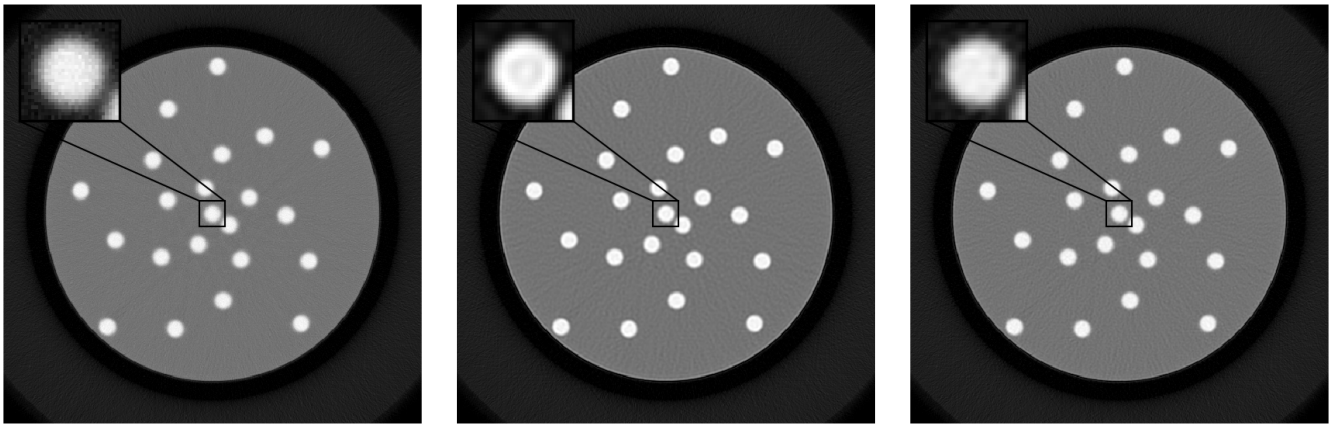

(b) Realistic trackers

Fig. 9. pCT reconstruction of the spiral phantom: without deconvolution (left), with deconvolution without uncertainty underestimation (middle), and with underestimation (right), for ideal trackers (top) and realistic trackers (bottom). The zoomed inset represents the central bead. The range of the grayscale of the image is $[0 - 2.2]$, and that of the inset is $[0.9 - 2.2]$.

the object is more homogeneous than with ideal trackers, and we deem global parameters sufficient in that case.

For the anthropomorphic phantoms, differences between the reconstructions and the reference were observed mainly along edges (Figure 11), and were caused by a lack of resolution or the presence of overshoot artifacts. For a rising edge, we have an overestimation followed by an underestimation if the spatial resolution is not optimal, and the opposite (underestimation followed by an overestimation) in the case of an overshoot due to deconvolution (Figure 4). A small RMSE represents an adequate trade-off between spatial resolution and overshoot.

The reconstructions of the ICRP phantom took into account tracker resolution to provide a realistic scenario. Our results showed a visible improvement of spatial resolution, with a reduced RMSE near the edges in all cases. In the case of the lung phantom, when no underestimation of the uncertainty was applied, the gain in spatial resolution was countered by an error due to overshoot artifacts (e.g. near the spine in Figure 11). With the underestimated convolution kernel, no overshoot was visible and the error due to spatial resolution was reduced everywhere. In the case of the head phantom, the RMSE was reduced for both deconvolutions, i.e. with $\beta = 1$ and $\beta = 0.7$, compared to the non-deblurred image, but the results were better for the case without underestimation ($\beta = 1$). We note that the scaling parameter β was chosen based on the results for the spiral phantom and applied to both anthropomorphic phantoms. Given that the path uncertainty values in the head were smaller than in the spiral phantom (maximum uncertainty of 0.8 mm in the head against 1.5 mm in the spiral), and that overshoot artifacts appear for high uncertainty values, it is likely that indeed no overshoot correction was needed for the head phantom. The maximum uncertainty for the lung phantom was 1.8 mm, which is closer to that of the spiral phantom. On the other hand, given that the path uncertainty was computed assuming homogeneous water, and that protons traversed a certain amount of air in the lung phantom, the uncertainty in the lung might be overestimated. In this case, underestimating the deconvolution kernel might correct for

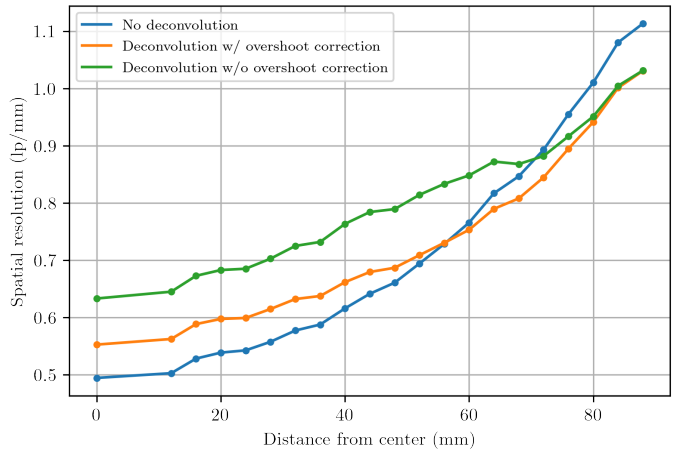

(a) Ideal trackers

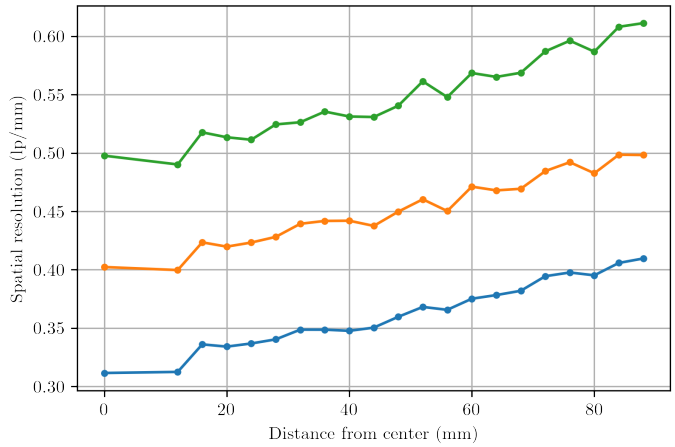

(b) Realistic trackers

Fig. 10. Spatial resolution in the spiral phantom as a function of the distance from the center. The results without overshoot correction correspond to $\beta = 1$ and $\alpha = 0.2$, and those with overshoot correction to $\beta = 0.7$ and $\alpha = 0.2$.

this overestimation, and explain why the results for the lung phantom with $\beta = 0.7$ were better. A different MLP formalism taking into account heterogeneities would help to compute more accurate uncertainty maps. The methods proposed to compute a heterogeneous MLP [20], [21] require knowledge about the tissue composition which can be obtained by iteratively updating the tissue composition from the current image in the case of an iterative reconstruction method. Alternatively, using an energy-adaptive parametrization of the MLP [22] might improve the path uncertainty estimation by providing a better estimate of the $1/p^2(E)v^2(E)$ term, which is currently approximated with a polynomial fitted to energy loss simulations in water. Still, in both slices and for all tested pairs (α, β), the measured RMSE indicates that the potential bias induced by deconvolution is still below the error due to low spatial resolution. As mentioned earlier, overshoot artifacts are object-dependent. Ultimately, in human-like geometries, they are expected to be less structured and therefore more benign than in the spiral phantom, as our results seem to indicate.

In this work, we have chosen to perform the deconvolution in the projection space to minutely take into account the spatial variation of the path uncertainty. However, it could be possible to do the deconvolution in the image space after reconstruction, especially in the case of realistic trackers for which the spatial variation of the uncertainty values is not as high as for ideal trackers. In an image domain deconvolution, we would need to approximate the uncertainty value in each pixel of the reconstructed image via a backprojection of the uncertainty maps, and then solve the same type of system as in Equation 20, only in two dimensions for a single slice. For one reconstructed image slice, one would perform one two-dimensional deconvolution as opposed to separate one-dimensional deconvolutions per projection, as in the current work. We expect that, in objects with little variation of the path uncertainty among projections, image-based deconvolution might provide similar results as projection-based deconvolution.

This work was conducted using a distance-driven projection binning algorithm, however, it can also be used with other direct methods [23]–[26] by deconvolving projections or partial backprojections. While other factors such as the reconstruction algorithm might affect spatial resolution, their impact is limited compared to MCS and tracker resolution [5]. Direct application of our deconvolution method to iterative reconstruction methods is not straightforward because it is projection-based. The authors of a previous study [8] included path uncertainty in their projection model to iteratively reconstruct a pCT image. Surprisingly, their results did not show any improvement of spatial resolution. The projection deconvolution method described in this work could also be used to reconstruct a better starting iterate for an iterative reconstruction algorithm including path uncertainty. Alternatively, an image-based deconvolution as discussed above could be done independently of the reconstruction method.

V. Conclusion

The purpose of this work was to investigate whether including path uncertainty in a deconvolution framework might improve spatial resolution in direct pCT reconstruction. It was shown that including path uncertainty to perform deconvolution of blurred distance-driven projections can significantly increase spatial resolution of pCT images when using realistic trackers. Particularly, the resolution in a water cylinder of 20 cm diameter with aluminium inserts was increased by up to 29% without introducing overshoot artifacts. Reconstructions of anthropomorphic phantoms also showed an enhancement of spatial resolution when tracker resolution was included in the MLP model. Deconvolution artifacts were less prominent for anthropomorphic images, and our results indicate that their impact on RSP accuracy might be lower than that of a poor spatial resolution.

Acknowledgments

The work of Feriel Khellaf and Nils Krah was partially supported by the project DIC20161236452 of the *Fondation pour la Recherche Médicale* (FRM). This work was performed within the framework of the SIRIC LYriCAN

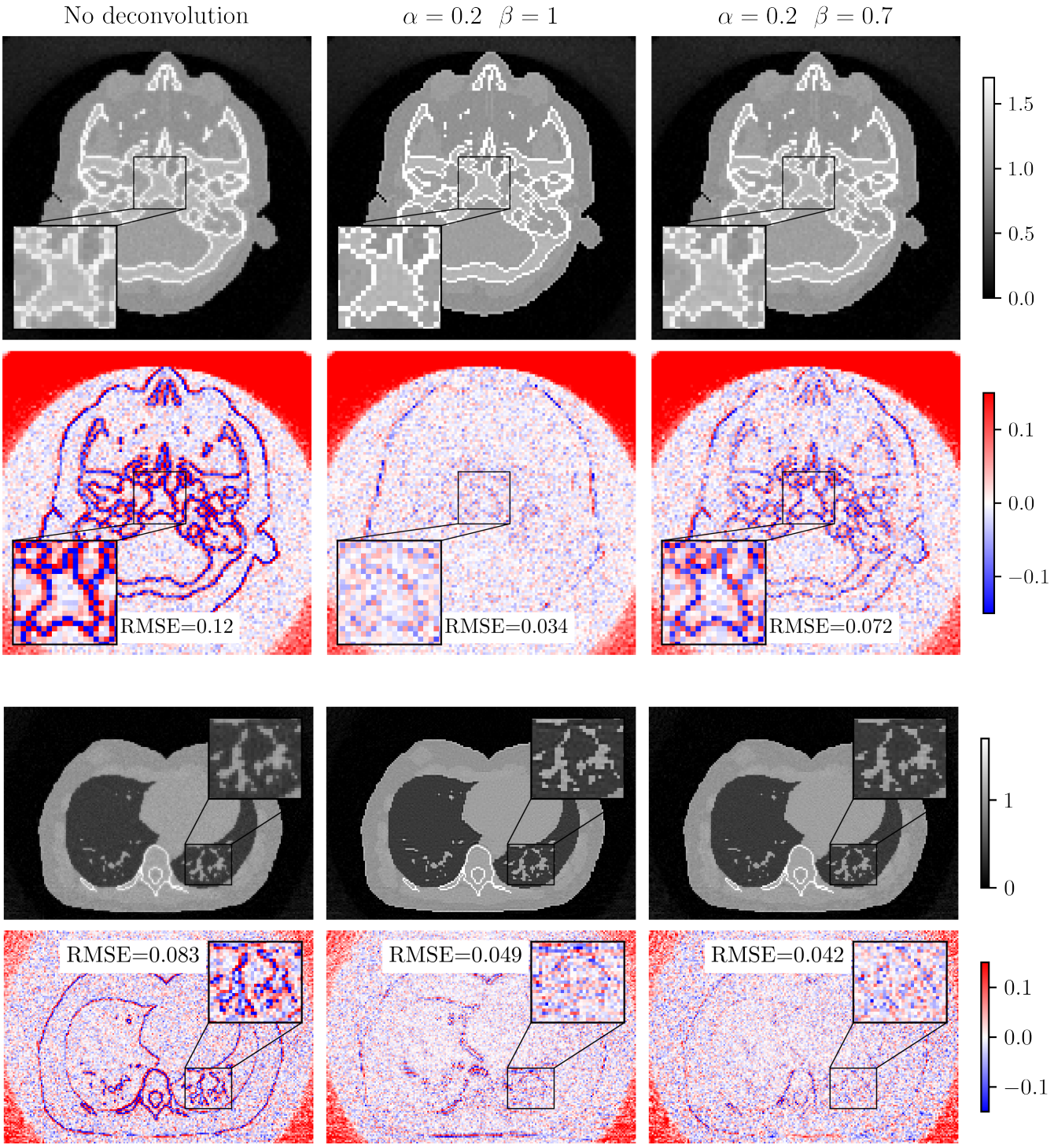

Fig. 11. Reconstruction of the head and lung slices using realistic trackers, and difference maps with the reference RSP images. The root mean square error (RMSE) is calculated inside the zoomed regions-of-interest.

INCa_INSERM_DGOS_12563 and the LABEX PRIMES (ANR-11-LABX-0063) of Université de Lyon, within the program "Investissements d'Avenir" (ANR-11-IDEX-0007) operated by the French National Research Agency (ANR). All authors declare that they have no known conflicts of interest in terms of competing financial interests or personal relationships that could have an influence or are relevant to the work reported in this paper.

REFERENCES

[1] R. P. Johnson, "Review of medical radiography and tomography with proton beams," *Reports on Progress in Physics*, vol. 81, no. 1, p. 016701, nov 2018.

[2] R. Schulte, V. Bashkirov, T. Li, Z. Liang, K. Mueller, J. Heimann, L. R. Johnson, B. Keeney, H.-W. Sadrozinski, A. Seiden *et al.*, "Conceptual design of a proton computed tomography system for applications in proton radiation therapy," *IEEE Transactions on Nuclear Science*, vol. 51, no. 3, pp. 866–872, 2004.

[3] R. Schulte, S. Penfold, J. Tafas, and K. Schubert, "A maximum likelihood proton path formalism for application in proton computed tomography," *Medical physics*, vol. 35, no. 11, pp. 4849–4856, 2008.

[4] T. Li, Z. Liang, J. V. Singanallur, T. J. Satogata, D. C. Williams, and R. W. Schulte, "Reconstruction for proton computed tomography by tracing proton trajectories: A Monte Carlo study," *Medical physics*, vol. 33, no. 3, pp. 699–706, 2006.

[5] F. Khellaf, N. Krah, J.-M. Letang, C.-A. Collins-Fekete, and S. Rit, "A comparison of direct reconstruction algorithms in proton computed tomography," *Physics in Medicine & Biology*, vol. 65, no. 10, p. 105010, 2020.

[6] Y. Censor, K. E. Schubert, and R. W. Schulte, "Developments in mathematical algorithms and computational tools for proton CT and particle therapy treatment planning," *IEEE Transactions on Radiation and Plasma Medical Sciences*, 2021.

[7] D. Williams, "The most likely path of an energetic charged particle through a uniform medium," *Physics in Medicine & Biology*, vol. 49, no. 13, p. 2899, 2004.

[8] D. Wang, T. R. Mackie, and W. A. Tomé, "On the use of a proton path probability map for proton computed tomography reconstruction a," *Medical physics*, vol. 37, no. 8, pp. 4138–4145, 2010.

[9] S. Rit, G. Dedes, N. Freud, D. Sarrut, and J. Létang, "Filtered backprojection proton CT reconstruction along most likely paths," *Med Phys*, vol. 40, no. 3, p. 031103, 2013.

[10] N. Krah, F. Khellaf, J. M. Létang, S. Rit, and I. Rinaldi, "A comprehensive theoretical comparison of proton imaging set-ups in terms of spatial resolution," *Physics in Medicine & Biology*, vol. 63, no. 13, p. 135013, 2018.

[11] A. Rahmim, J. Qi, and V. Sossi, "Resolution modeling in PET imaging: theory, practice, benefits, and pitfalls," *Medical physics*, vol. 40, no. 6Part1, p. 064301, 2013.

[12] S. Tong, A. M. Alessio, K. Thielemans, C. Stearns, S. Ross, and P. E. Kinahan, "Properties and mitigation of edge artifacts in PSF-based PET reconstruction," *IEEE Transactions on Nuclear Science*, vol. 58, no. 5, pp. 2264–2275, 2011.

[13] S. Stute and C. Comtat, "Practical considerations for image-based PSF and blobs reconstruction in PET," *Physics in Medicine & Biology*, vol. 58, no. 11, p. 3849, 2013.

[14] J. Nuyts, "Unconstrained image reconstruction with resolution modelling does not have a unique solution," *EJNMMI physics*, vol. 1, no. 1, pp. 1–7, 2014.

[15] B. Bai and P. D. Esser, "The effect of edge artifacts on quantification of positron emission tomography," in *IEEE Nuclear Science Symposuim & Medical Imaging Conference*. IEEE, 2010, pp. 2263–2266.

[16] S. Jan, D. Benoit, E. Becheva, T. Carlier, F. Cassol, P. Descourt, T. Frisson, L. Grevillot, L. Guigues, L. Maigne *et al.*, "Gate v6: a major enhancement of the gate simulation platform enabling modelling of CT and radiotherapy," *Physics in Medicine & Biology*, vol. 56, no. 4, p. 881, 2011.

[17] ICRP, *Adult Reference Computational Phantoms*, ser. ICRP Publication 110. Ann. ICRP 39 (2), 2009.

[18] V. A. Bashkirov, R. P. Johnson, H. F.-W. Sadrozinski, and R. W. Schulte, "Development of proton computed tomography detectors for applications in hadron therapy," *Nuclear Instruments and Methods in Physics Research Section A: Accelerators, Spectrometers, Detectors and Associated Equipment*, vol. 809, pp. 120–129, 2016.

[19] S. Richard, D. B. Husarik, G. Yadava, S. N. Murphy, and E. Samei, "Towards task-based assessment of CT performance: system and object MTF across different reconstruction algorithms," *Medical physics*, vol. 39, no. 7Part1, pp. 4115–4122, 2012.

[20] C.-A. Collins-Fekete, E. Bär, L. Volz, H. Bouchard, L. Beaulieu, and J. Seco, "Extension of the Fermi–Eyges most-likely path in heterogeneous medium with prior knowledge information," *Physics in Medicine & Biology*, vol. 62, no. 24, p. 9207, 2017.

[21] M. D. Brooke and S. N. Penfold, "An inhomogeneous most likely path formalism for proton computed tomography," *Physica Medica*, vol. 70, pp. 184–195, 2020.

[22] N. Krah, D. Dauvergne, J. M. Létang, S. Rit, and E. Testa, "Energy-adaptive calculation of the most likely path in proton CT," *Physics in Medicine & Biology*, 2021.

[23] G. Poludniowski, N. Allinson, and P. Evans, "Proton computed tomography reconstruction using a backprojection-then-filtering approach," *Physics in Medicine & Biology*, vol. 59, no. 24, p. 7905, 2014.

[24] S. Rit, R. Clackdoyle, J. Hoskovec, and J. M. Létang, "List-mode proton CT reconstruction using their most likely paths via the finite Hilbert transform of the derivative of the backprojection," in *The 13th International Meeting on Fully Three-Dimensional Image Reconstruction in Radiology and Nuclear Medicine*, ser. Fully3D 2015 Conference Proceedings, 2015, pp. 324–327.

[25] C.-A. Collins-Fekete, S. Brousmiche, S. K. Portillo, L. Beaulieu, and J. Seco, "A maximum likelihood method for high resolution proton radiography/proton CT," *Physics in Medicine & Biology*, vol. 61, no. 23, p. 8232, 2016.

[26] F. Khellaf, N. Krah, J. M. Létang, and S. Rit, "2D directional ramp filter," *Physics in Medicine & Biology*, vol. 65, no. 8, p. 08NT01, 2020.